Chapter 3

Nonlinear Interaction Between Vortex and Wave in Rotating Shallow Water

Norihiko Sugimoto

Additional information is available at the end of the chapter

http://dx.doi.org/10.5772/65431

Abstract

This chapter is primarily concerned with the generation of inertia-gravity wave by vortical flows (spontaneous emission) in shallow water system on an *f*-plane. Sound waves are generated from vortical flows (aeroacoustics). There are many theoretical and numerical works regarding this subject. A shallow water system is equivalent to a two-dimensional adiabatic gas system, if the effect of Earth's rotation is negligibly small. Then gravity waves are analogous to sound waves. While it is widely known that the effect of the Earth's rotation suppresses inertia-gravity wave radiation, there are few studies about spontaneous emission in rotating shallow water. Here, the generation of inertia-gravity waves by unsteady vortical flows is investigated analytically and numerically as an extension of aeroacoustics. A background of this subject is introduced briefly and several recent works including new results are reviewed. Main findings are cyclone-anticyclone asymmetry in spontaneous emission and a local maximum of intensity of gravity waves emitted from anticyclones at intermediate value of the Coriolis parameter *f*, which are caused by the source originating in the Coriolis acceleration. All different experimental settings show the similar results, suggesting the robustness of these features.

Keywords: geophysical fluid dynamics, inertia-gravity wave, spontaneous emission, shallow water flows, aeroacoustics

1. Introduction

Sound waves are generated from vortical flows (aeroacoustics). After the pioneering work of Lighthill [1], many theoretical and numerical works regarding this subject have been done. There are several good review papers and text books, for example, see [2–5].

Inertia-gravity waves, in which buoyancy and Coriolis force provide the restoring force, are important in the atmosphere and ocean, because they drive general circulation in the middle

atmosphere [6] and contribute to the ocean energy budget [7, 8]. Traditionally, rotating shallow water system has been used to study nonlinear interactions between vortex and wave [9] because this system is the simplest system in which both vortical flows and inertia-gravity waves can exist. One of the typical examples is the Rossby adjustment process [10, 11], in which initial unbalanced state is assumed. Then inertia-gravity waves (hereafter inertia-gravity waves are referred to gravity waves) are radiated from unbalanced state toward balanced state. However, there are few works regarding the generation of gravity waves by unsteady motions of nearly balanced vortical flows in rotating shallow water system.

Ford's pioneering work [12] has shown that gravity waves are radiated from unsteady vortical flows. This type of gravity wave radiation is referred to as "spontaneous emission" [13], because initial balanced flows radiate gravity waves spontaneously during the time evolution. Since a shallow water system is equivalent to a two-dimensional adiabatic gas system if the effect of Earth's rotation is negligibly small, gravity waves are analogous to sound waves. Using the acoustic analogy of Lighthill [1], Ford [12, 13] introduced a source of gravity waves. For the purpose of practical motivation, this new paradigm of spontaneous emission is intensively investigated; for example, see [14] and references therein. Recently, the theory of generation mechanism has been proposed [15, 16]. While it is pointed out that spontaneous emission in the shallow water system is different from that in the continuous stratified system [17], fundamental works from a viewpoint of geophysical fluid dynamics are nevertheless important [18].

As an extension of Ford's works [12, 13], several numerical works are performed in shallow water system on an *f*-plane [19, 20] and a sphere [21]. While it is widely known that the effect of the Earth's rotation suppresses inertia-gravity wave radiation, previous studies [20, 21] have reported that the effect of the Earth's rotation intensify gravity wave radiation in some parameter space. In this chapter, recent results of the inertia-gravity wave radiation from nearly balanced vortical flows as an extension of sound wave generation from vortical flows are reviewed. Inertia-gravity wave radiation from various types of vortical flows, such as a corotating vortex pair [22], elliptical vortex (Kirchhoff vortex) [23] and merging of (equal or unequal) vortices [24, 25], are investigated in a wide range of parameter space. All these works have reported that cyclone-anticyclone asymmetry in spontaneous emission and a local maximum of intensity of gravity waves emitted from anticyclones at intermediate value of the Coriolis parameter *f*.

This chapter is organized as follows. In Section 2, the analytical derivation of the far fields of gravity waves is introduced for the cases of a corotating point vortex pair and an almost circular Kirchhoff vortex. The derived forms are verified quite well by the numerical simulation (Section 3). In addition, the results of gravity wave radiation from the merging of (equal or unequal) vortices are also introduced. Section 4 gives brief summary points and future issues.

2. Analytical estimate

In this section, the analytical derivation of the far fields of gravity waves from vortical flows is introduced. The derived form includes the effect of Earth's rotation in the source term, which

http://dx.doi.org/10.5772/65431

causes the cyclone-anticyclone asymmetry. Two examples of the corotating point vortex pair and Kirchhoff vortex are shown. See Refs. [22] and [23] for details.

2.1. Basic equation

Basic equations are the shallow water equations on an *f*-plane, written as

$$\frac{\partial u_c}{\partial t} + u_c \frac{\partial u_c}{\partial x} + v_c \frac{\partial u_c}{\partial y} - f v_c = -g \frac{\partial h}{\partial x}, \tag{1}$$

$$\frac{\partial v_c}{\partial t} + u_c \frac{\partial v_c}{\partial x} + v_c \frac{\partial v_c}{\partial y} + f u_c = -g \frac{\partial h}{\partial y}, \tag{2}$$

$$\frac{\partial h}{\partial t} + u_c \frac{\partial h}{\partial x} + v_c \frac{\partial h}{\partial y} + h\left(\frac{\partial u_c}{\partial x} + \frac{\partial v_c}{\partial y}\right) = 0, \tag{3}$$

where $\boldsymbol{u} = (u_c, v_c)$ is the horizontal velocity vector, where u_c and v_c are the velocity components in the x and y directions in the Cartesian coordinates, respectively. The total depth of the fluid $h = \eta + h_0$, in which η is the surface displacement from the average depth of the fluid h_0. The Coriolis parameter and gravitational acceleration are f and g, respectively.

Eqs. (1)–(3) are the same as for vortex sound (aeroacoustics) if the effect of the Earth's rotation is negligibly small. From Eqs. (1)–(3), Lighthill-Ford equation is obtained [1, 12]:

$$\left(\frac{\partial^2}{\partial t^2} + f^2 - c_0^2 \nabla^2\right) \frac{\partial h}{\partial t} = \frac{\partial^2}{\partial x_i \partial x_j} T_{ij}, \tag{4}$$

where $x_1 = x$, $x_2 = y$ and the Einstein summation convention is used. Note that $c_0 = \sqrt{gh_0}$ and ∇^2 are the phase speed of the fastest gravity wave and the horizontal Laplacian, respectively. Here, T_{ij} is written as

$$T_{ij} = \frac{\partial (h u_i u_j)}{\partial t} + \frac{f}{2}(\epsilon_{ik} h u_j u_k + \epsilon_{jk} h u_i u_k) + \frac{g}{2}\frac{\partial}{\partial t}(h - h_0)^2 \delta_{ij}, \tag{5}$$

where $\epsilon_{12} = -\epsilon_{21} = 1$, $\epsilon_{11} = \epsilon_{22} = 0$, $u_1 = u_c$, $u_2 = v_c$ and δ_{ij} is the Kronecker delta. Since the left-hand side of Eq. (4) is the wave operator of a linear gravity wave, the right-hand side can be regarded as the source of gravity waves under the assumption in the limit of small Froude number [12, 13], Fr (where $Fr \equiv U/c_0$ is the ratio of the flow velocity U to the phase speed of gravity waves). Note that Fr corresponds to Mach number (the ratio of the flow velocity to the phase speed of sound waves) in the field of aeroacoustics.

2.2. Source and far field

In the source T_{ij}, the primary source of gravity waves for the nonrotating case is the first term on the right-hand side of Eq. (5), which is associated with the vortical flows. Then, for the relevant term on the right-hand side of Eq. (4), the following approximation holds

$$\frac{\partial^2(hu_iu_j)}{\partial x_i \partial x_j} \approx h_0 \nabla\cdot(\boldsymbol{\omega}\times\boldsymbol{u}) + h_0\nabla^2\left(\frac{1}{2}u^2\right), \tag{6}$$

for nondivergent flow ($\nabla\cdot u = 0$ and $h \approx h_0$) under the assumption of $Fr \ll 1$ with compact source of the vortical motion. The second term on the right-hand side of Eq. (6) can be neglected, because this term is $O(Fr^2)$ smaller than that from the first term for $Fr \ll 1$.

For the rotating case, on the other hand, the second term on the right-hand side of Eq. (5) becomes also important for relatively larger f [20, 21]. Then, for the relevant term on the right-hand side of Eq. (4), the following approximation holds

$$\frac{\partial^2}{\partial x_i \partial x_j}\frac{f}{2}(\epsilon_{ik}hu_ju_k + \epsilon_{jk}hu_iu_k) = \frac{\partial^2}{\partial x_i \partial x_j} fh\epsilon_{ik}u_ju_k \approx -fh_0\nabla\cdot[\boldsymbol{k}\times(\boldsymbol{\omega}\times\boldsymbol{u})], \tag{7}$$

for nondivergent flow ($\nabla\cdot\mathbf{u} = 0$ and $h \approx h_0$). This is the source originating in the Coriolis acceleration.

The Green's function of Eq. (4) in the two-dimensional domain incorporating time variation is defined from the Klein-Gordon equation:

$$\left(\nabla^2 - \frac{1}{c_0^2}\frac{\partial^2}{\partial t^2} - \mu^2\right)G_2(\boldsymbol{x}, t, \boldsymbol{x}', t') = -\delta(\boldsymbol{x} - \boldsymbol{x}')\delta(t - t'), \tag{8}$$

where $\mu = f/c_0$. The form of Green's function is

$$G_2(\boldsymbol{x}, t, \boldsymbol{x}', t') = \frac{c_0}{2\pi}\frac{\cos\left(\mu\sqrt{c_0^2(t-t')^2 - |x-x'|^2}\right)}{\sqrt{c_0^2(t-t')^2 - |x-x'|^2}}\theta_s\left(c_0(t-t') - |\boldsymbol{x} - \boldsymbol{x}'|\right), \tag{9}$$

where θ_s is the Heaviside function. Finally, by analogy with the derivation of the far field of sound waves, the integral form of far field of gravity waves is formally expressed as

$$\frac{\partial h(x,t)}{\partial t} = \frac{h_0}{c_0^2}\iiint_{-\infty}^{\infty} G_2\left[\frac{\partial}{\partial t'}\nabla\cdot(\boldsymbol{\omega}\times\boldsymbol{u}) - f\nabla\cdot[\boldsymbol{k}\times(\boldsymbol{\omega}\times\boldsymbol{u})]\right]\mathrm{d}x'\,\mathrm{d}t'. \tag{10}$$

2.3. Typical examples

To solve Eq. (10) analytically, two cases of a corotating point vortex pair and an almost circular Kirchhoff vortex are introduced as examples. **Figure 1** shows the schematics of these experimental configurations.

A point vortex pair with the same sign and strength corotates. For aeroacoustics, analytical [4] and numerical [26] studies are performed in this configuration. Zeitlin [9] also derived an analytical solution in nonrotating shallow water. A vortex pair with a circulation Γ positioned at distance $2l$ corotates at an angular velocity $\Omega = \Gamma/4\pi l^2$. The positions are

http://dx.doi.org/10.5772/65431

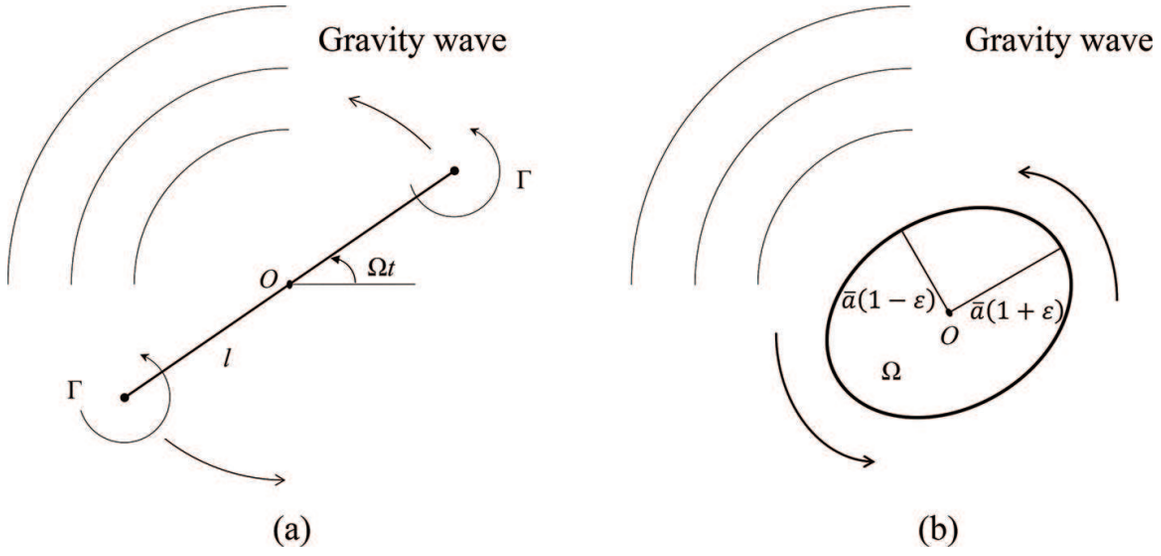

Figure 1. Schematics of experimental configurations for the cases of (a) a corotating point vortex pair and (b) an almost circular Kirchhoff vortex.

$$\boldsymbol{x} = (x_1, x_2) = \boldsymbol{s} \equiv \Big(s_1(t), s_2(t)\Big) = \pm l\Big(\cos(\Omega t),\, \sin(\Omega t)\Big). \tag{11}$$

Then the vorticity $\boldsymbol{\omega}$ and velocity $\boldsymbol{u} = (u_1, u_2)$ associated with the vortices are written as

$$\boldsymbol{\omega} = \Gamma \boldsymbol{k}[\delta(\boldsymbol{x} - \boldsymbol{s}) + \delta(\boldsymbol{x} + \boldsymbol{s})], \tag{12}$$

$$\boldsymbol{u} = \pm\Omega \boldsymbol{k} \times \boldsymbol{s} \text{ at } \boldsymbol{x} = \pm\boldsymbol{s}, \tag{13}$$

where $\boldsymbol{k}$ is a unit vector in the z direction and δ is a delta function. Assuming that the characteristic velocity scale $U = \Omega l \ll c_0$, then,

$$\boldsymbol{\omega} \times \boldsymbol{u} = -\Gamma \Omega \boldsymbol{s}[\delta(\boldsymbol{x} - \boldsymbol{s}) - \delta(\boldsymbol{x} + \boldsymbol{s})]. \tag{14}$$

From Eq. (6) the source associated with vortical flows is equivalent to the two-dimensional quadrupole

$$\nabla \cdot (\boldsymbol{\omega} \times \boldsymbol{u}) \approx \frac{\partial^2}{\partial x_i \partial x_j}\Big(S_{ij}\delta(\boldsymbol{x})\Big), \tag{15}$$

where

$$S_{ij} = \Gamma \Omega l^2 \begin{pmatrix} 1 + 2\cos 2\Omega t & \sin 2\Omega t \\ \sin 2\Omega t & 1 - \cos 2\Omega t \end{pmatrix}. \tag{16}$$

Similarly, from Eq. (7) the source originating in the Coriolis acceleration is expressed as

$$-f \nabla \cdot [\boldsymbol{k} \times (\boldsymbol{\omega} \times \boldsymbol{u})] \approx f \frac{\partial^2}{\partial x_i \partial x_j}\Big(\epsilon_{ik} S_{kj} \delta(\boldsymbol{x})\Big). \tag{17}$$

As for the case of the Kirchhoff vortex, the derivation is in the same line as a corotating point vortex pair. The Kirchhoff vortex has a patch of constant vorticity, Ω, inside an ellipse and zero vorticity outside. It is an exact solution of the two-dimensional, incompressible and inviscid flow equations [27]. Howe [4] derived far field of sound waves from the Kirchhoff vortex analytically. An almost circular Kirchhoff vortex with a small aspect ratio is the ellipse defined by the polar equation for $\varepsilon \ll 1$

$$r = \overline{a}\left[1 + \varepsilon \cos\left(2\theta - \frac{\Omega t}{2}\right)\right], \tag{18}$$

where the semimajor axis of the ellipse is $a = \overline{a}(1+\varepsilon)$, the semiminor axis is $b = \overline{a}(1-\varepsilon)$. The ellipse rotates at angular velocity $\Omega/4$. The velocity within the core is

$$\boldsymbol{u} = (u_1, u_2) = -\frac{1}{2}\Omega r\left(\sin\theta + \varepsilon \sin\left(\theta - \frac{\Omega t}{2}\right), -\cos\theta + \varepsilon\cos\left(\theta - \frac{\Omega t}{2}\right)\right). \tag{19}$$

Then, to first order in ε, the source associated with vortex and the source originating in the Coriolis acceleration are again expressed as Eqs. (15) and (17), respectively, where

$$S_{ij} = \frac{\varepsilon\pi\Omega^2\overline{a}^4}{8}\begin{pmatrix} \cos(\Omega t/2) & \sin(\Omega t/2) \\ \sin(\Omega t/2) & -\cos(\Omega t/2) \end{pmatrix}. \tag{20}$$

After substituting Eqs. (15) and (17) in Eq. (10), the delta function can be integrated

$$\frac{\partial h(\boldsymbol{x},t)}{\partial t} = \frac{h_0}{c_0^2}\frac{\partial^2}{\partial x_i \partial x_j}\int_{-\infty}^{\infty} G_2\left[\frac{\partial}{\partial t'}(S_{ij}) + f\epsilon_{ik}S_{kj}\right]\mathrm{d}t'. \tag{21}$$

Recalling that the following approximation in the far field ($r = \sqrt{x_1^2 + x_2^2} \gg 1$),

$$\frac{\partial^2}{\partial x_i \partial x_j} = \left(\frac{\delta_{ij}}{r} - \frac{x_i x_j}{r^3}\right)\frac{\partial}{\partial r} + \frac{x_i x_j}{r^2}\frac{\partial^2}{\partial r^2} \approx \frac{x_i x_j}{r^2}\frac{\partial^2}{\partial r^2}, \tag{22}$$

then it follows from Eq. (21):

$$\begin{aligned}\frac{\partial h(\boldsymbol{x},t)}{\partial t} &= \frac{h_0}{c_0^2}\frac{\partial^2}{\partial r^2}\int_{-\infty}^{\infty} G_2\frac{x_i x_j}{r^2}\left[\frac{\partial}{\partial t'}(S_{ij}) + f\epsilon_{ik}S_{kj}\right]\mathrm{d}t' \\ &= \begin{cases} \dfrac{2\Gamma\Omega^2 l^2 h_0}{c_0^2}\left(1 - \dfrac{f}{2\Omega}\right)\dfrac{\partial^2}{\partial r^2}\displaystyle\int_{-\infty}^{\infty} G_2 \sin(2\theta - 2\Omega t')dt', & \text{for } a \text{ corotating vortex pair} \\ \dfrac{\varepsilon\pi\Omega^3\overline{a}^4 h_0}{16c_0^2}\left(1 - \dfrac{2f}{\Omega}\right)\dfrac{\partial^2}{\partial r^2}\displaystyle\int_{-\infty}^{\infty} G_2 \sin\left(2\theta - \dfrac{\Omega t'}{2}\right)dt', & \text{for the Kirchhoff vortex.} \end{cases}\end{aligned} \tag{23}$$

With the form of Green's function Eq. (9), Eq. (23) for a corotating vortex pair is written as

http://dx.doi.org/10.5772/65431

$$\frac{\partial h(\boldsymbol{x},t)}{\partial t}=\left(1-\frac{f}{2\Omega}\right)\frac{\Gamma\Omega^2l^2h_0}{\pi c_0}\frac{\partial^2}{\partial r^2}\underbrace{\int_{-\infty}^{t}\frac{\sin\left(2\theta-2\Omega t'\right)\cos\left(\mu\sqrt{\tau}\right)}{\sqrt{\tau}}\theta_s\Big(c_0(t-t')-r\Big)\mathrm{d}t'}_{B}, \tag{24}$$

where $\tau=c_0^2(t-t')^2-r^2$. The integral in Eq. (24), labeled as B, can be calculated by changing variables, $t-t'=(r/c_0)\cosh\varphi$ and $\sqrt{\tau}=\sinh\varphi$. By using the integral form of Hankel's function $\boldsymbol{H}_0(x)$, B is expressed as

$$\begin{aligned}B=&\frac{1}{2c_0}\mathrm{Re}\left[\mathrm{i}\pi\boldsymbol{H}_0^{(1)}\left(r\sqrt{\left(\frac{2\Omega}{c_0}\right)^2-\mu^2}\right)\right]\sin\left(2\theta-2\Omega t\right)\\&-\mathrm{sgn}(f)\mathrm{sgn}(\Omega)\frac{1}{2c_0}\mathrm{Im}\left[\mathrm{i}\pi\boldsymbol{H}_0^{(1)}\left(r\sqrt{\left(\frac{2\Omega}{c_0}\right)^2-\mu^2}\right)\right]\cos\left(2\theta-2\Omega t\right),\end{aligned} \tag{25}$$

where the sign function $\mathrm{sgn}(x)$ is defined so that $\mathrm{sgn}(0)=1$. $\boldsymbol{H}_2^{(1)}(\alpha x)\approx-\boldsymbol{H}_0^{(1)}(\alpha x)$ for $\alpha x\gg1$ are also used for $(r/c_0)\sqrt{\Omega^2/4-f^2}\gg1$. Then the following approximation can be used

$$\frac{\partial^2B}{\partial r^2}\approx\left[\left(\frac{\Omega}{2c_0}\right)^2-\mu^2\right]B, \tag{26}$$

because $d^2\boldsymbol{H}_0^{(1)}(\alpha x)/dx^2=\alpha^2/2\Big(\boldsymbol{H}_2^{(1)}(\alpha x)-\boldsymbol{H}_0^{(1)}(\alpha x)\Big)\approx-\alpha^2\boldsymbol{H}_0^{(1)}(\alpha x)$. Finally, the following form for the far field of gravity waves is obtained for a corotating point vortex pair,

$$\begin{aligned}\frac{\partial h(\boldsymbol{x},t)}{\partial t}=&\frac{2\Gamma\Omega^4l^2h_0}{c_0^4}\left(1-\frac{f}{2\Omega}\right)\left[1-\left(\frac{f}{2\Omega}\right)^2\right]\left[\boldsymbol{Y}_0\left(\frac{r}{c_0}\sqrt{4\Omega^2-f^2}\right)\sin\left(2\theta-2\Omega t\right)\right.\\&\left.-\mathrm{sgn}(f)\mathrm{sgn}(\Omega)\boldsymbol{J}_0\left(\frac{r}{c_0}\sqrt{4\Omega^2-f^2}\right)\cos\left(2\theta-2\Omega t\right)\right],\end{aligned} \tag{27}$$

where $\boldsymbol{H}_0^{(1)}(\alpha x)=\boldsymbol{J}_0(\alpha x)+\mathrm{i}\boldsymbol{Y}_0(\alpha x)$ is used, in which $\boldsymbol{J}_0$ and $\boldsymbol{Y}_0$ are the zeroth-order Bessel functions of the first and second kind, respectively. The similar procedure from Eqs. (24) to (27) can be applied for the Kirchhoff vortex, then

$$\begin{aligned}\frac{\partial h(\boldsymbol{x},t)}{\partial t}=&\frac{\varepsilon\pi\Omega^5\overline{a}^4h_0}{256c_0^4}\left(1-\frac{2f}{\Omega}\right)\left[1-\left(\frac{2f}{\Omega}\right)^2\right]\left[\boldsymbol{Y}_0\left(\frac{r}{c_0}\sqrt{\frac{\Omega^2}{4}-f^2}\right)\sin\left(2\theta-\frac{\Omega}{2}t\right)\right.\\&\left.-\mathrm{sgn}\ (f)\ \mathrm{sgn}\ (\Omega)\ \boldsymbol{J}_0\left(\frac{r}{c_0}\sqrt{\frac{\Omega^2}{4}-f^2}\right)\cos\left(2\theta-\frac{\Omega}{2}t\right)\right].\end{aligned} \tag{28}$$

Eqs. (27) and (28) are applicable for both cyclone ($\Omega > 0$) and anticyclone ($\Omega < 0$) vortices regardless of the signs of f. In the absence of the Earth's rotation for $f \to 0$, Eqs. (27) and (28) correspond to the analytical form of the vortex sound [4, 26]. In contrast, there are several important effects for finite f. First, spontaneous emission is suppressed for large f because of a small value in the square root and second parentheses. Second, the source Eq. (7) originating in the Coriolis acceleration acts oppositely to the gravity wave radiation caused by the second term in the first parentheses. Meanwhile, the source Eq. (7) originating in the Coriolis acceleration cancels out the source Eq. (6) associated with vortex, since the same signs of Ω and f for cyclone. In contrast, those two sources magnify each other for anticyclone. Then, gravity waves are intensely radiated from anticyclone. Simple explanations for the suppression of gravity wave radiation at large f are reported [9]. Note also that it is possible to derive analytical estimate in the case of evanescent gravity waves for $\Omega^2/4 \le f^2$ [22].

Examples of the far field of gravity waves ($d\Phi/dt$, where $\Phi \equiv gh$ is the geopotential height) from the corotating point vortex pair and Kirchhoff vortex are shown in **Figure 2**. Here, the Rossby number ($Ro \equiv U_l/fL$) and Froude number ($Fr \equiv U_l/\sqrt{\Phi_0}$) are defined by the typical values, where the velocity U_l and the length L scales are chosen as the velocity and the length of each vortex configuration. The values of $\Omega = 0.1$, $U_l = 0.5$, $l = 1.0$ and $\Phi_0 = 25/36$ for the corotating vortex pair and those of $U_l = 0.2$, $L = a = 1.0$ and $\Phi_0 = 4/9$ for the Kirchhoff vortex are fixed to be consistent with those of numerical simulations. The value of $\Omega = 0.449 - 0.025(0.95 - b)$ for the Kirchhoff vortex is also chosen for different values of b in order to keep $U_l = 0.2$ as a constant value. The double spiral patterns for both cases clearly show the rotating quadrupole features of the radiated gravity waves. The wave patterns depend on the vortical flows and their parameter values, namely, Ω, Ro, Fr and the aspect ratio. Anticyclone radiates gravity waves more intensely than cyclone at relatively large f (**Figure 2a** and **b**) and there is no cyclone-anticyclone asymmetry in spontaneous emission for the nonrotating case of $f = 0$ (**Figure 2c**).

The intensity of gravity waves for both cases of the corotating vortex pair, I_{vp} and the Kirchhoff vortex, I_{kv}, are defined by

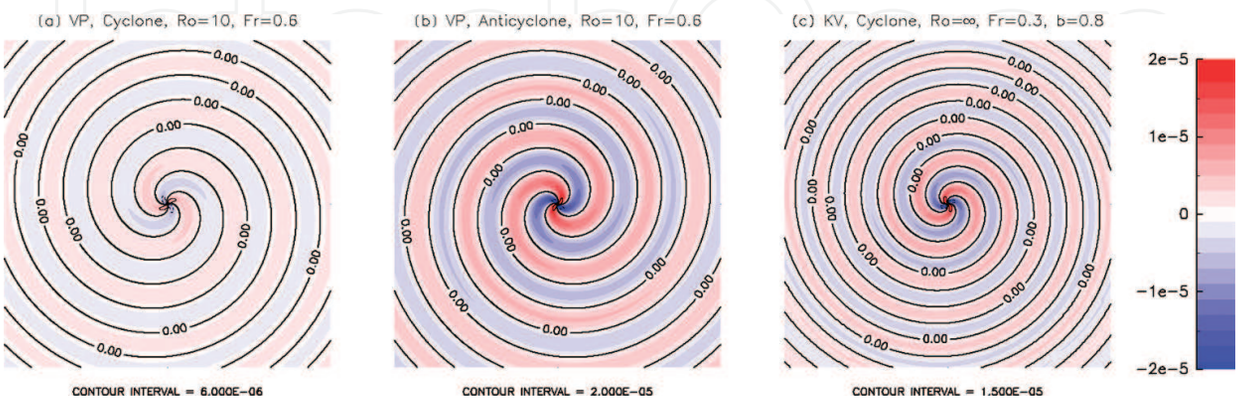

Figure 2. Snapshots of the far fields ($r \le 100$) of gravity waves ($d\Phi/dt$, where $\Phi \equiv gh$) radiated from the corotating point vortex pair and Kirchhoff vortex: (a) cyclone, (b) anticyclone corotating vortex pair with $Ro = 10$ ($f = 1/10$) and $Fr = 0.6$ ($gh_0 = 25/36$) and (c) cyclone Kirchhoff vortex with $Ro = \infty$ ($f = 0$), $b = 0.8$ ($\bar{a} = 0.9, \varepsilon = 1/9$) and $Fr = 0.3$ ($gh_0 = 4/9$).

http://dx.doi.org/10.5772/65431

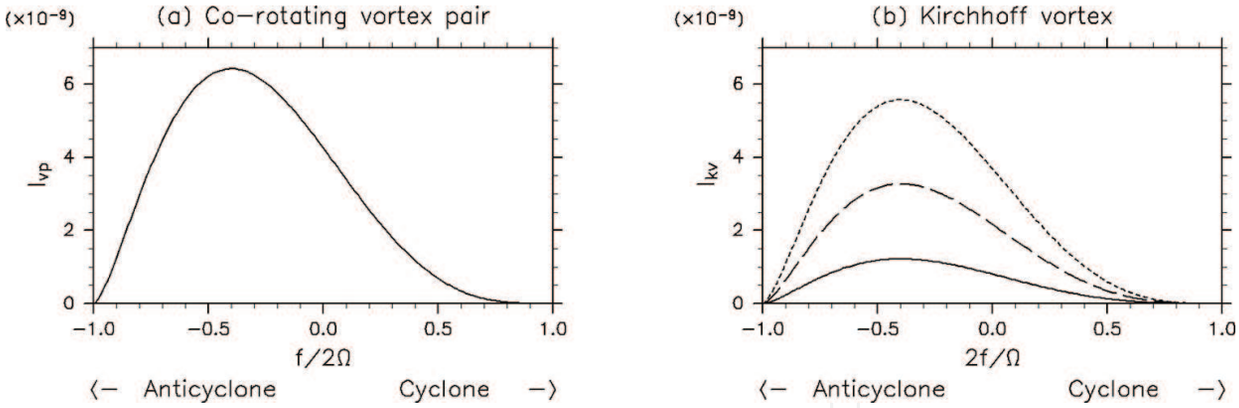

Figure 3. Analytical estimates of the dependence on f of the intensity of gravity waves: (a) the corotating vortex pair, I_{vp}, calculated from Eq. (29) and (b) the Kirchhoff vortex, I_{kv}, calculated from Eq. (30) with $b = 0.95$ ($\bar{a} = 0.975, \varepsilon = 1/39$; solid line), $b = 0.9$ ($\bar{a} = 0.95, \varepsilon = 1/19$; broken line) and $b = 0.8$ ($\bar{a} = 0.9, \varepsilon = 1/9$; dotted line).

$$I_{vp} = \int_0^{2\pi} \left(\frac{\partial \Phi}{\partial t}\right)^2 r d\theta \approx \frac{64\pi^2\Omega^9 l^8}{c_0^3}\left(1 - \frac{f}{2\Omega}\right)^2 \left[1 - \left(\frac{f}{2\Omega}\right)^2\right]^{\frac{3}{2}}, \tag{29}$$

$$I_{kv} \approx \frac{\varepsilon^2\pi^2\Omega^9\bar{a}^8}{16384c_0^3}\left(1 - \frac{2f}{\Omega}\right)^2 \left[1 - \left(\frac{2f}{\Omega}\right)^2\right]^{\frac{3}{2}}, \tag{30}$$

to estimate the dependence on f of gravity waves from both cyclone and anticyclone. Here, $\boldsymbol{J}_0(\alpha x) \approx \sqrt{2/\pi\alpha x}\cos(\alpha x - \pi/4)$ and $\boldsymbol{Y}_0(\alpha x) \approx \sqrt{2/\pi\alpha x}\sin(\alpha x - \pi/4)$ for $\alpha x \gg 1$ are used to derive Eqs. (29) and (30). These values are the same at any r in the field. **Figure 3** shows I_{vp} (Eq. 29) and I_{kv} (Eq. 30) for three b cases ($b = 0.95, 0.9,$ and 0.8). For anticyclone vortex, a local maximum appears at $f/2\Omega = -0.4$ (Ro ~ 12.5, f ~ 2/25) for the corotating point vortex pair and $2f/\Omega = -0.4$ (Ro ~ 1, f ~ 1/10) for the Kirchhoff vortex. The cyclone-anticyclone asymmetry is similar to both cases, though vortical flows are completely different. Note that Ro is different among the vortices for the same value of f because the velocity and length scales depend on the vortical configuration.

3. Numerical simulation

To verify the analytical solution, a numerical simulation with a newly developed spectral method in an unbounded domain has been performed. The numerical results are in excellent agreement with the analytical results of Eqs. (27) and (28) [22, 23]. Furthermore, additional numerical simulations have been performed for the cases of merging of (equal or unequal) vortices, in which analytical solution cannot be derived [24, 25]. In this section, the results of numerical simulation as well as model settings are introduced.

3.1. Model settings

Shallow water equations on an *f*-plane in polar coordinates are used for the numerical simulation. The equations of relative vorticity ζ, divergence δ and geopotential height Φ are

$$\frac{\partial \zeta}{\partial t} = -\frac{1}{r}\frac{\partial (rv\zeta_a)}{\partial r} - \frac{1}{r}\frac{\partial (u\zeta_a)}{\partial \theta}, \tag{31}$$

$$\frac{\partial \delta}{\partial t} = \frac{1}{r}\frac{\partial (ru\zeta_a)}{\partial r} - \frac{1}{r}\frac{\partial (v\zeta_a)}{\partial \theta} - \Delta(E+\Phi), \tag{32}$$

$$\frac{\partial \Phi}{\partial t} = -\frac{1}{r}\frac{\partial (rv\Phi)}{\partial r} - \frac{1}{r}\frac{\partial (u\Phi)}{\partial \theta}, \tag{33}$$

where u and v are the velocities in the azimuthal (θ) and radial (r) directions, respectively and

$$\text{relative vorticity } \zeta = \frac{1}{r}\frac{\partial (ru)}{\partial r} - \frac{1}{r}\frac{\partial v}{\partial \theta} = \Delta\psi, \tag{34}$$

$$\text{divergence } \delta = \frac{1}{r}\frac{\partial (rv)}{\partial r} + \frac{1}{r}\frac{\partial u}{\partial \theta} = \Delta\chi, \tag{35}$$

$$\text{Laplacian } \Delta = \frac{1}{r}\frac{\partial}{\partial r}\left(r\frac{\partial}{\partial r}\right) + \frac{1}{r^2}\frac{\partial^2}{\partial \theta^2}, \tag{36}$$

$$\text{kinetic energy } E = \frac{1}{2}(u^2+v^2), \tag{37}$$

$$\text{absolute vorticity } \zeta_{\mathrm{a}} = f + \zeta, \tag{38}$$

where ψ and χ are the stream function and velocity potential, respectively.

Eqs. (31)–(33) are solved by a conformal mapping from a sphere $P_i(\lambda,\phi)$ with radius R to a plane $Q_i(r,\theta)$ in the numerical simulation [28]. **Figure 4** shows a schematic of this mapping. With the aid of the following relation,

$$r = 2R\tan\left(\frac{\phi}{2} + \frac{\pi}{4}\right), \tag{39}$$

the transformation of the coordinates is expressed as

$$\frac{\partial}{\partial r} = \frac{1-\sin\phi}{2R}, \frac{1}{r}\frac{\partial}{\partial \theta} = \frac{1-\sin\phi}{2R\cos\phi}\frac{\partial}{\partial \lambda}. \tag{40}$$

Then the phenomena on a two-dimensional unbounded plane can be calculated on a sphere with an ordinary spectral method of spherical harmonics by this mapping. Since grid points are arranged nonuniformly (many grid points are positioned in the near field of vortical flows, while few are in the far field of gravity waves), this method enables us to simulate nonlinear interactions between vortical flows and gravity waves with high accuracy [22–25].

http://dx.doi.org/10.5772/65431

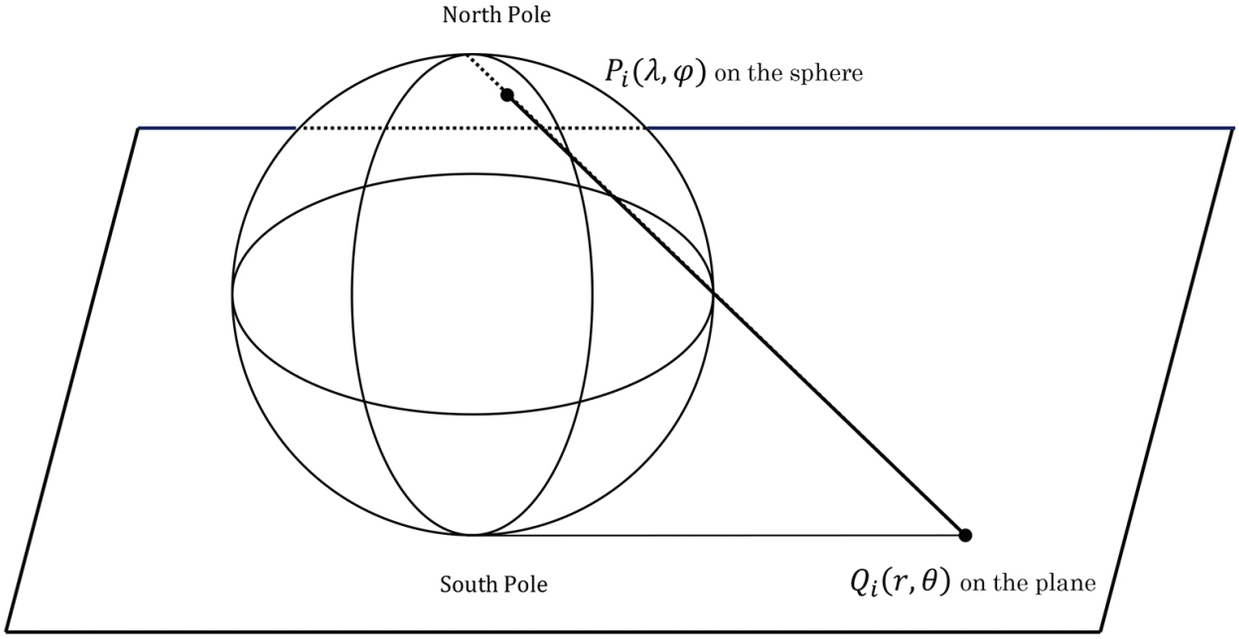

Figure 4. Schematic of the mapping method from $P_i(\lambda, \phi)$ on sphere to $Q_i(r, \theta)$ on a plane.

Additional advantage is that the term of the hyper viscosity, which is intended to dissipate unresolved small scales numerically in the spectral model, acts as a sponge layer. By the conformal mapping, the usual form of hyper viscosity can be written as

$$\nu(-1)^{p+1}\left(\frac{4\Delta}{(1-\sin\phi)^2}\right)^p P, \tag{41}$$

where ν, p and $P = (\zeta, \delta, \Phi)$ are the viscosity coefficient, order of viscosity and physical variables, respectively. Eq. (41) acts as a usual hyper viscosity in the near field of vortical flow for small ϕ. On the other hand, the viscosity becomes large and acts as a sponge layer for large ϕ in the far filed where waves are propagating. Eq. (41) is easy to code in the numerical simulation because Laplacian operator on a sphere is simply calculated by spherical harmonics.

3.2. Verification

As an initial state, a corotating Gaussian vortex pair is used to mimic a point vortices, which is expressed as

$$\zeta = \pm A_1 \exp\left\{-\frac{(x-x_1)^2+(y-y_1)^2}{2\sigma^2}\right\} \pm A_2 \exp\left\{-\frac{(x-x_2)^2+(y-y_2)^2}{2\sigma^2}\right\}, \tag{42}$$

where $(x, y) = (r\cos\theta, r\sin\theta)$. The values of A_1, A_2, σ, $(x_1, y_1) = (l\cos\theta_1, l\sin\theta_1)$ and $(x_2, y_2) = \Big(l\cos(\theta_1+\pi), l\sin(\theta_1+\pi)\Big)$ determine the amplitudes, radius and positions of the vortices, respectively (see also **Figure 1a**). The values of $A_1 = A_2 = 20$, $\sigma = 0.05$, $l = 0.5$ and

$\theta_1 = \pi/4$ are fixed and then the maximum velocity $U_{vp} \approx 0.5$ becomes a constant value. The Rossby number $Ro \equiv U_{vp}/fl$ and the Froude number $Fr \equiv U_{vp}/\sqrt{\Phi_0}$ are defined by the basic state, where Φ_0 = 25/36 determines the average depth. Then, $Fr(= 0.6)$ is fixed and Ro is reciprocal of f. The field of Φ is set to be in gradient balance with ζ.

Similarly, elliptical Gaussian vortex positioned at the origin is used to mimic the Kirchhoff vortex

$$\zeta = \pm A \exp\left\{ -\left(\frac{\sqrt{(ax)^2 + (by)^2}}{l_{kv}} \right)^n \right\}, \tag{43}$$

where A, a, b, n and l_{kv} determines the amplitude, the length of semimajor axis and semiminor axis, the steepness and the core area of elliptical vortex, respectively. The values of $a = 1.0$, $n = 10,$ and $l_{kv} = 1.0$ are fixed, then the semimajor axis of elliptical vortex is fixed to ~1, while b is swept to change the aspect ratio. Then, $\overline{a}$ and ε are determined by b solely (see also **Figure 1b**). $A = 0.449 - 0.025(0.95 - b)$ is also set to keep the maximum velocity $U_{kv} \approx 0.2$ as a constant value. The Rossby number $Ro \equiv U_{kv}/fl_{kv}$ and the Froude number Fr $\equiv U_{kv}/\sqrt{\Phi_0}$ are defined by the basic state, where Φ_0 = 4/9 determines the average depth. Again, $Fr(= 0.3)$ is fixed and Ro is reciprocal of f. Note again that Ro is different among the vortices for the same value of f because the velocity and length scales depend on the vortical configuration. The field of Φ is set to be in gradient balance with ζ, too. **Figure 5** shows examples of initial Gaussian vortex pair with $Ro = 10$ $(f = 1/10)$ and $Fr = 0.6$ and elliptical Gaussian vortex with $Ro = 1$ $(f = 1/10)$, $Fr = 0.3$ and $b = 0.9$ $(\overline{a} = 0.95, \varepsilon = 1/19)$. The vorticity ζ, velocity u in the θ direction and geopotential height Φ are shown for the corotating vortex pair (along the section of center of the vortices) and for the elliptical vortex (along the sections of semimajor axis and semiminor axis of the vortex).

The number of grid points is set to be 2048 × 1024 in the θ and r directions, with the truncation wavenumber of spherical harmonics $T = 682$ and $R = 8$. Then the grid interval in the r direction (Δr) in the near field ($r \leq 2$) is $\Delta r \leq 0.0249$ and the farthest grid points are positioned at r ~ 13,632. The viscosity coefficient and order of viscosity are set to be $\nu = 10^{-11}$ and p= 3, respectively. Fourth-order Runge-Kutta method is used for the time integration. For the corotating vortex pair 8,000 total time steps are conducted to the end of time 200 with a time interval $\Delta t = 0.025$, while for the elliptical vortex, 10,000 time steps are conducted with a $\Delta t = 0.02$.

In both configurations, the numerical simulations with several Ro for fixed Fr are performed for cyclone and anticyclone vortex individually, starting from above initial state. Gravity waves are spontaneously radiated from both cyclone and anticyclone vortical flows for large enough Ro, while anticyclones rotate in the opposite direction to cyclones. **Figure 6** shows line plots of radiated gravity waves $d\Phi/dt$ against r from cyclone and anticyclone for both cases of the corotating vortex pair and Kirchhoff vortex. The line plots in the $\theta = \pi/4$ section at $t = 200$ are shown for the numerical simulation (broken lines), while appropriate times are chosen for the analytical estimates (solid lines) to coincide with the numerical results. The amplitudes of

http://dx.doi.org/10.5772/65431

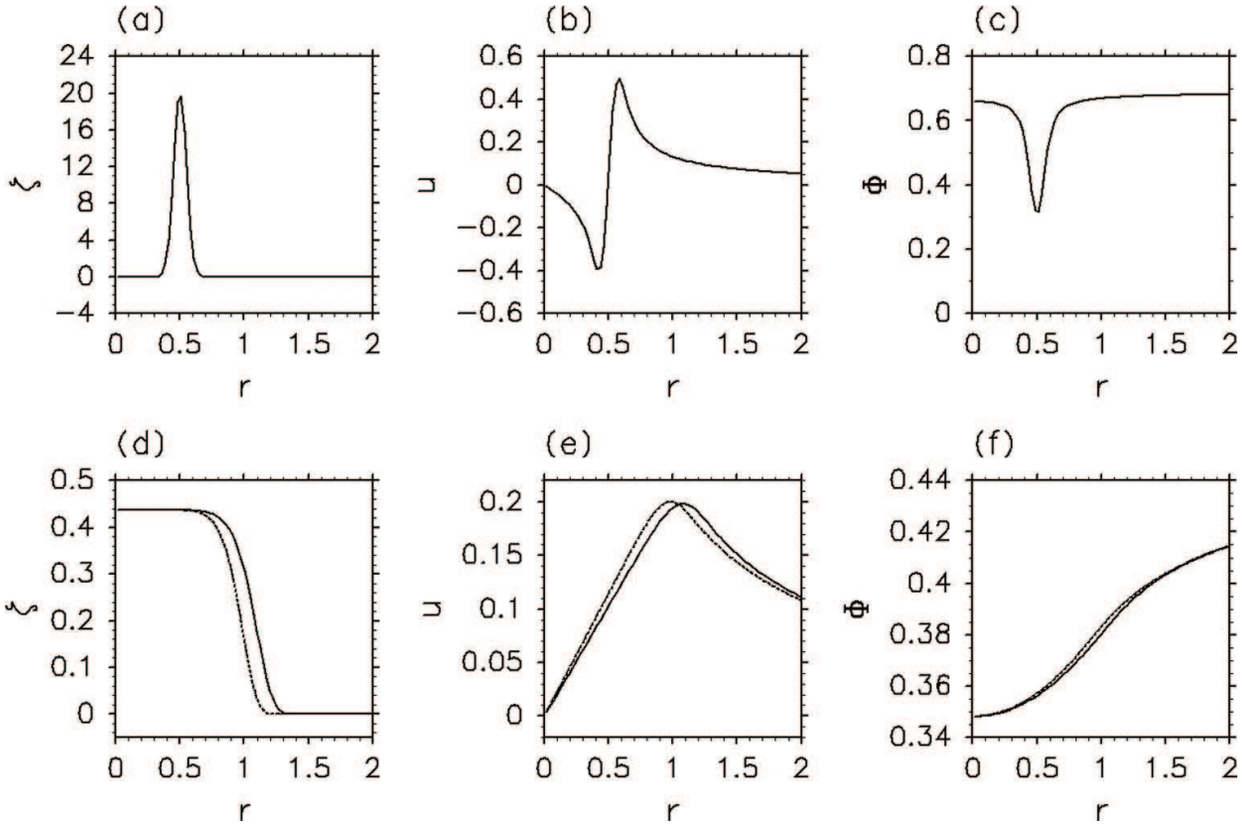

Figure 5. Initial corotating cyclone vortex pair (top panels) with $Ro = 10$ $(f = 1/10)$ and $Fr = 0.6$ ($\Phi_0 = 25/36$) and elliptical cyclone vortex (bottom panels) with $Ro = 1$ $(f = 1/10)$, $Fr = 0.3$ ($\Phi_0 = 4/9$) and $b = 0.9$ ($\overline{a} = 0.95, \varepsilon = 1/19$): ζ (a, d), u (b, e) and Φ (c, f) are shown. In the top panels, solid lines indicate the values along the section of center of vortex. In bottom panels, the solid lines indicate the values along the section of semi-major axis, while dotted lines indicate those of semi-minor axis.

gravity waves in the far field between the analytical and numerical results are almost the same for all cases. While there is no cyclone–anticyclone asymmetry for the nonrotating case ($f = 0$), the anticyclones radiate gravity waves more intensely than cyclones for relatively small Ro cases. Local maximum appears around $2f/\Omega \sim -0.4$ only for the cases of anticyclone, as expected in Section 2.3. All cases with different Ro are remarkably good overlapped between analytical estimates and numerical results, except for the elliptical vortex with for $b = 0.8$.

The intensity of gravity waves for both cases calculated from Eqs. (29) and (30) in the numerical simulation agree well with analytical estimates (not shown). The results indicate that the analytical estimates give the far fields of gravity waves quite accurately and the newly developed numerical model is well verified. Furthermore, cyclone-anticyclone asymmetry and the local maximum of gravity waves for anticyclone are also confirmed for both cases of the corotating vortex pair and Kirchhoff-like elliptical vortex. Note that for the elliptical vortex with for $b = 0.8$, the aspect ratio increases gradually in the time evolution, more elongated elliptical vortex with filaments appears. Then the amplitude of the source becomes larger than that used in the analytical estimate. Significant deviation for the shape of vortex from the ideal elliptical vortex causes the large discrepancy between the analytical and numerical results for $b = 0.8$ [23].

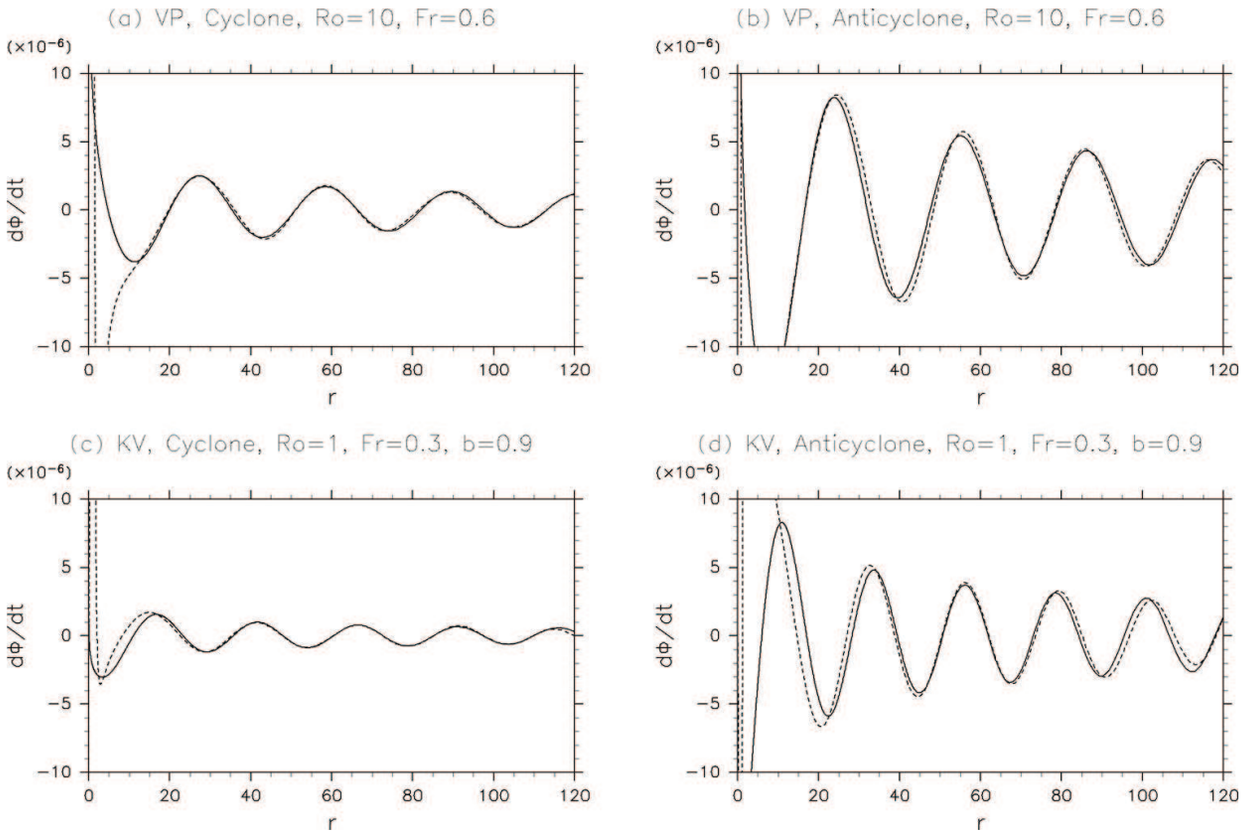

Figure 6. The far filed ($r \leq 100$) of gravity waves ($d\Phi/dt$) for the corotating vortex pair (top panels) with $Ro = 10$ and $Fr = 0.6$ and elliptical vortex (bottom panels) with $Ro = 1$, $Fr = 0.3$, and $b = 0.9$. The analytical estimates Eqs. (27) and (28) (solid lines) and the numerical results in the $\theta = \pi/4$ section at $t = 200$ (broken lines) are shown for (a, c) cyclones and (b, d) anticyclones.

3.3. Extended experiments

As extended experiments, the results of the merging of (equal and unequal) vortices are introduced here [24, 25]. As an initial state, a pair of corotating Gaussian vortices expressed by Eq. (42) with different values of $A_1 = 2.165$, $\sigma = 0.16$ is used. By defining asymmetric parameter $d \equiv A_2/A_1$, $d = 1.0$ is used for the symmetric vortex merger, while $d < 1.0$ is swept for asymmetric vortex merger. The Rossby number $Ro \equiv U_{vm}/fl$ and the Froude number $Fr \equiv U_{vm}/\sqrt{\Phi_0}$ are defined by the basic state again, where $U_{vm} \approx 0.2$ is the maximum velocity (fixed). The average depth is set to $\Phi_0 = 4/9$ so that $Fr = 0.3$ (fixed). Then, again, Ro is reciprocal of f. The field of Φ is set to be in gradient balance with ζ. **Figure 7** shows initial Gaussian vortex (cyclone) with $Ro = 4$ ($f = 1/10$) and $Fr = 0.3$ for symmetric ($d = 1.0$) and asymmetric merger ($d = 0.7$). The other experimental settings are the same as Subsection 3.2.

Starting from above initial state, vortices evolve with time. The time evolutions for cyclones with $Ro = 4$ and $Fr = 0.3$ for the symmetric ($d = 1.0$) and asymmetric merger ($d = 0.7$) are shown in **Figure 8**. Vortices merge in a similar way for both cases of equal vortices and unequal vortices. Initially, vortices corotate with each other ($t \lesssim 45$) and then merge into a single vortex ($45 \lesssim t \lesssim 65$). After merging, the vortex rotates with nutation from an elliptical shape to an axisymmetric one ($65 \lesssim t$). Spontaneous emission is observed at all three stages, while amplitude

http://dx.doi.org/10.5772/65431

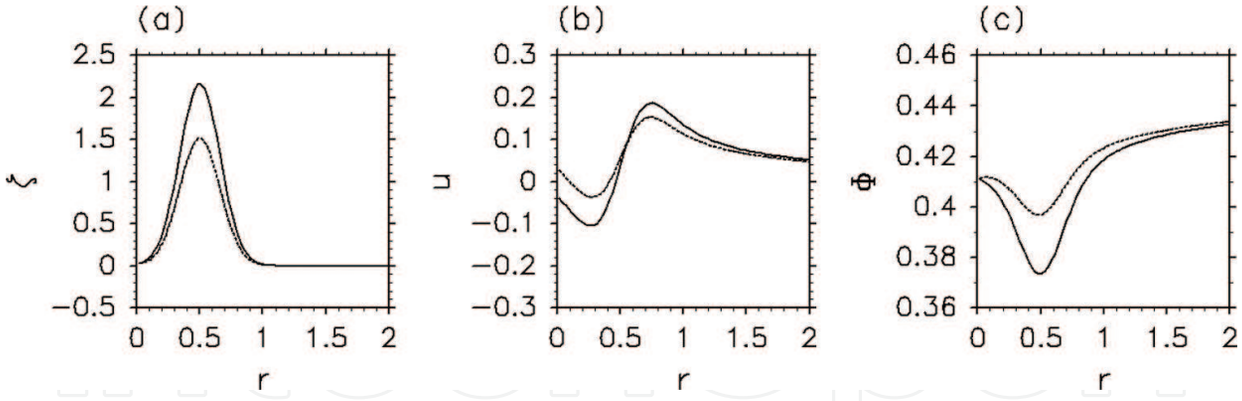

Figure 7. Initial Gaussian cyclone vortex pair with $Ro = 4$ $(f = 1/10)$ and $Fr = 0.3$ for symmetric ($d = 1.0$, solid line) and asymmetric merger ($d = 0.7$, dotted line): ζ (a), u (b) and Φ (c) are shown. One (weaker) vortex is shown (for unequal vortices).

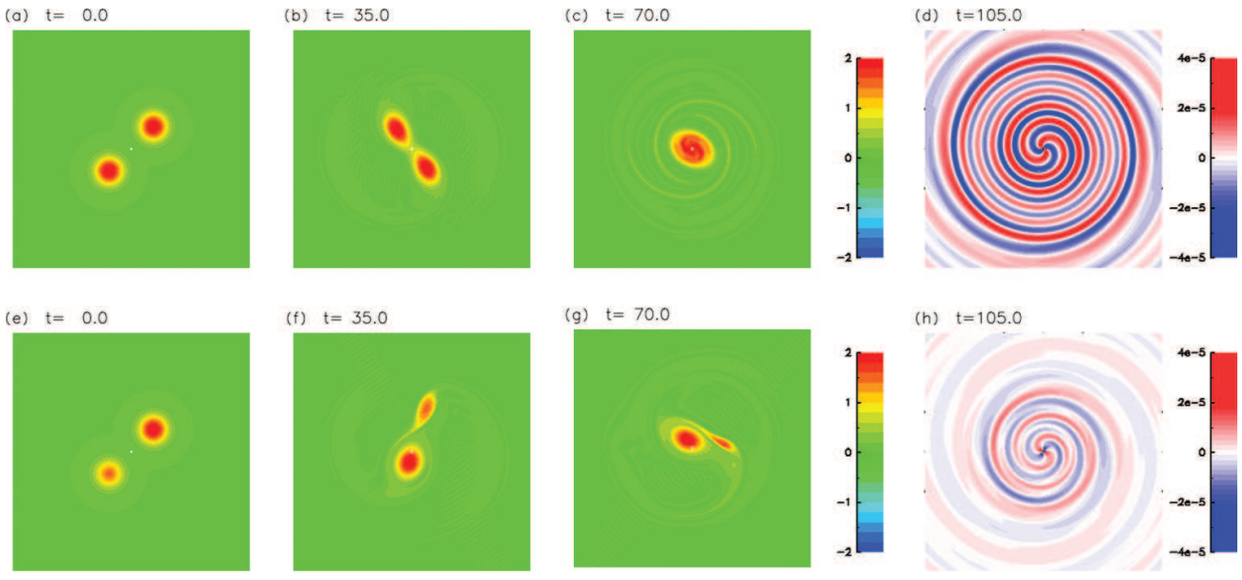

Figure 8. Snapshots of the time evolution of cyclones with $Ro = 4$ $(f = 1/10)$ and $Fr = 0.3$ for symmetric merger ($d = 1.0$, top panels) and asymmetric merger ($d = 0.7$, bottom panels): ζ for (a, e) $t = 0$, (b, f) $t = 45$, (c, g) $t = 90$ and $\partial\Phi/\partial t$ for (d, h) $t = 135$ (d). ζ is shown in the near field ($r \leq 2$), while $\partial\Phi/\partial t$ is shown in the far field ($r \leq 50$).

of gravity waves for the asymmetric merger is significantly smaller than that of the symmetric merger. The wavelength of the gravity waves from the corotating vortices becomes shorter gradually with time due to an increase of the rotation rate. Then it becomes almost constant after merging into a single vortex.

A series of numerical simulations at different values of Ro $(0.5 \leq Ro \leq \infty)$ is performed. The time evolutions of $\partial\Phi/\partial t$ at several r values are shown in **Figure 9** for both cyclones and anticyclones with $Ro = 4$ and $Fr = 0.3$ for the symmetric ($d = 1.0$) and asymmetric merger ($d = 0.7$). While vortical flows evolve with time in a similar manner (not shown), gravity waves radiated from them are considerably different between cyclones and anticyclones. At large $Ro(\geq 4)$, both cyclones and anticyclones radiate gravity waves in the three stages of vortical flows:

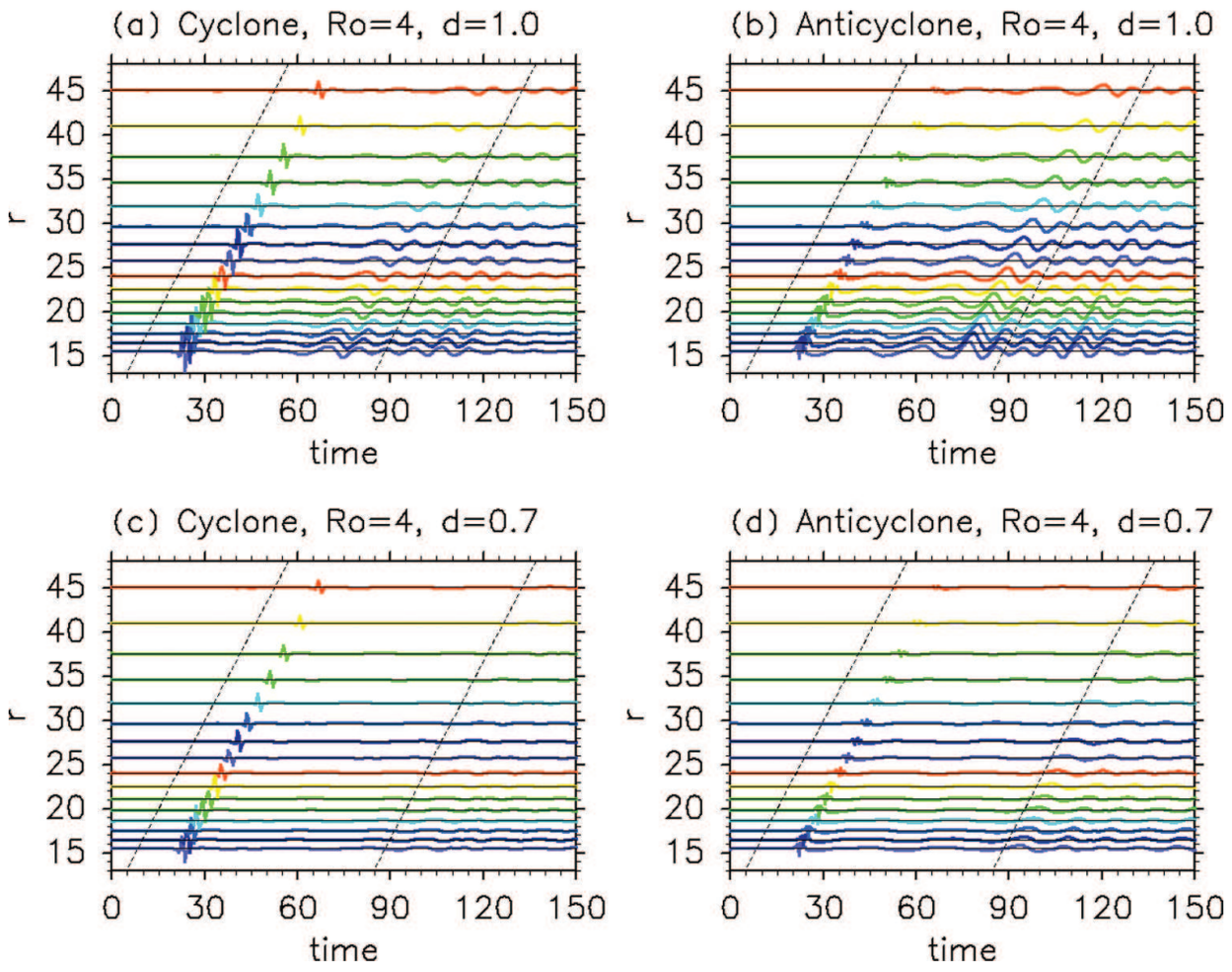

Figure 9. Time evolutions of $\partial\Phi/\partial t$ (colored lines multiplied by 10^4) from symmetric merger (top panels) and asymmetric merger (bottom panels) wtih $Ro = 4$ and $Fr = 0.3$: (a, c) cyclone and (b, d) anticyclone. Black dotted lines indicate the phase speed of the fastest gravity waves.

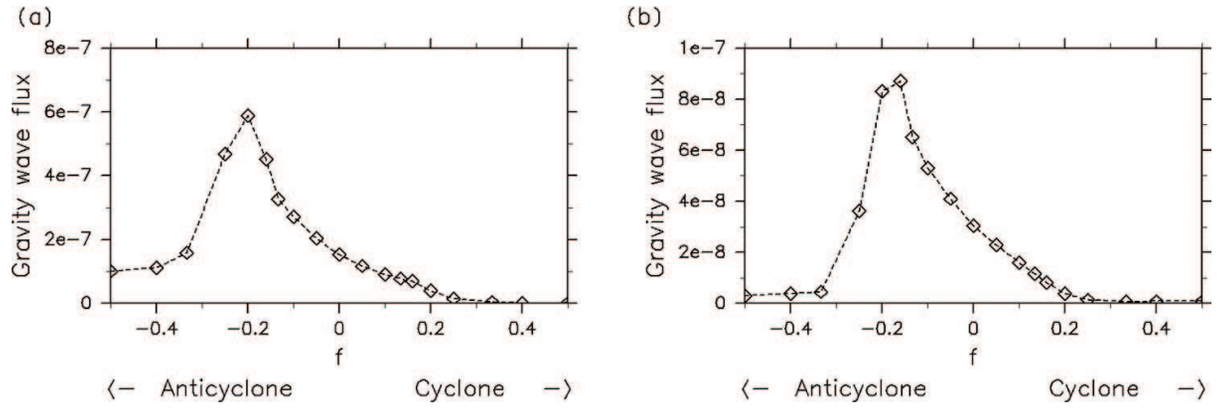

Figure 10. Dependence on f of the maximum value of the gravity wave flux averaged in the θ direction at $r = 45$ for the (a) symmetric merger and (b) asymmetric merger.

corotating ($t \lesssim 45$), merging ($45 \lesssim t \lesssim 65$) and after merging ($65 \lesssim t$). At smaller $Ro(\leq 0.8)$, however, gravity waves from cyclones decrease significantly. There are almost no gravity waves, except for the initial geostrophic adjustment. On the other hand, gravity waves from

anticyclones are radiated even when gravity waves from corotating vortices are hardly observed, namely, spontaneous emission is observed after merging into a single vortex. Therefore, significant cyclone-anticyclone asymmetry appears at small *Ro*.

In order to estimate the intensity of gravity waves quantitatively, a pseudo-energy flux is derived and calculated as the gravity wave flux [12, 21]. This quantity is conserved when gravity waves propagate into the far field. **Figure 10** shows the maximum values of the gravity wave flux averaged in the θ direction at $r = 45$ for several *Ro* values ($0.5 \leq Ro \leq \infty$). Generally, the maximum values are caused by gravity waves from the time of merging. Cyclone-anticyclone asymmetry is confirmed clearly. Anticyclones radiate gravity waves more intensely than cyclones and they have a local maximum of gravity wave flux at $f \sim 0.2$ for both cases. See Refs. [24] and [25] for details.

4. Concluding remarks

4.1. Summary points

1. Far field of inertia-gravity wave radiated from the corotating point vortex pair and Kirchhoff vortex with nearly circular shape is derived analytically in the *f*-plane shallow water system. Cyclone-anticyclone asymmetry in gravity waves from vortical flows and a local maximum of intensity of gravity waves from anticyclones at an intermediate *f* appear. This is caused by the effect of the Earth's rotation.
2. The derived analytical estimate is well verified for both cases of the corotating vortex pair and Kirchhoff vortex with a small aspect ratio by the numerical simulation with a newly developed spectral method in an unbounded domain.
3. The numerical experiments extend to the cases of symmetric and asymmetric vortex merger, in which analytical estimate cannot be derived. In both cases, cyclone-anticyclone asymmetry clearly appears and the local maximum at intermediate *f* exists only for anticyclones.
4. Within all parameter values and vortical flows used in the present work, there is a cyclone-anticyclone asymmetry at finite values of *f*. Gravity waves from anticyclones are larger than those from cyclones and have a local maximum at intermediate *f*. The source originating in the Coriolis acceleration has a key role in cyclone-anticyclone asymmetry in spontaneous emission. This feature would be robust and ubiquitous in the rotating shallow water system.

4.2. Future issues

1. The derived analytical forms would give useful references for testing the accuracy of the numerical model from a viewpoint of developing new numerical methods.
2. Cyclone-anticyclone asymmetry may be related with the change of the dominant balanced state from quasi-geostrophic one to gradient wind one [29].

3. There are additional effects which cause the discrepancy between analytical and numerical results, such as nutation of vortex, change of the rotation rate and filaments of the vortex.

4. More comprehensible understanding of cyclone-anticyclone asymmetry in spontaneous emission from general complicated vortical flows is needed not only in the rotating shallow water system but also in the continuous stratified system.

Acknowledgements

The work was supported by the JSPS Grant-in-Aid for Young Scientists (B) (no. 25800265). The GFD-DENNOU Library was used for drawing the figures. ISPACK-1.0.3 was used for numerical simulation and analysis. N.S. thanks K. Ishioka, H. Kobayashi, Y. Shimomura, P. D. Williams, R. Plougonven, M. E. McIntyre and the editor H. Pérez-de-Tejada for their constructive comments.

Author details

Norihiko Sugimoto

Address all correspondence to: nori@phys-h.keio.ac.jp

Department of Physics, Keio University, Yokohama, Japan

References

[1] M. J. Lighthill. On the sound generated aerodynamically. I. general theory. Proc. R. Soc. London. 1952;**211A**:564–587. DOI: 10.1098/rspa.1952.0060

[2] J. E. F. Williams. Aeroacoustics. Annu. Rev. Fluid Mech. 1977;**9**:447–468. DOI: 10.1146/annurev.fl.09.010177.002311

[3] M. E. Goldstein. Aeroacoustics of turbulent shear flows. Annu. Rev. Fluid Mech. 1984;**16**:263–285. DOI: 10.1146/annurev.fl.16.010184.001403

[4] M. S. Howe. Theory of vortex sound. Cambridge: Cambridge University Press; 2003. 216 p. DOI: 10.1017/CBO9780511755491

[5] M. Wang, J. B. Freund, S. K. Lele. Computational prediction of flow-generated sound. Annu. Rev. Fluid Mech. 2006;**38**:483–512. DOI: 10.1146/annurev.fluid.38.050304.092036

[6] D. C. Fritts, M. J. Alexander. Gravity wave dynamics and effects in the middle atmosphere. Rev. Geophys. 2003;**41**:1003. DOI: 10.1029/2001RG000106

[7] R. Ferrari, C. Wunsch. Ocean circulation kinetic energy: reservoirs, sources and sinks. Annu. Rev. Fluid Mech. 2009;**41**:253–282. DOI: 10.1146/annurev.fluid.40.111406.102139

[8] N. Sugimoto, R. Plougonven. Generation and backreaction of spontaneously emitted inertia-gravity waves. Geophys. Res. Lett..2016;**43**(7):3519–3525. DOI: 10.1002/2016GL068219

[9] V. Zeitlin. Nonlinear dynamics of rotating shallow water: Methods and Advances. Amsterdam: Elsevier; 2007. 392 p.

[10] C. G. Rossby. On the mutual adjustment of pressure and velocity distributions in certain simple current systems. II. J. Mar. Res. 1938;**5**:239–263.

[11] A. E. Gill. Adjustment under gravity in a rotating channel. J. Fluid Mech. 1977;**80**:641–671. DOI: 10.1017/S0022112076002280

[12] R. Ford. Gravity wave radiation from vortex trains in rotating shallow water. J. Fluid Mech. 1994;**281**:81–118. DOI: 10.1017/S0022112094003046

[13] R. Ford, M. E. McIntyre, W. A. Norton. Balance and the slow quasimanifold: some explicit results. J. Atmos. Sci. 2000;**57**:1236–1254. DOI: 10.1175/1520-0469(2000)057

[14] R. Plougonven, F. Zhang. Internal gravity waves from atmospheric jets and fronts. Rev. Geophys. 2014;**52**:33–76. DOI: 10.1002/2012RG000419

[15] Y. Yasuda, K. Sato, N. Sugimoto. A theoretical study on the spontaneous radiation of inertia-gravity waves using the renormalization group method. Part I: derivation of the renormalization group equations. J. Atmos. Sci. 2015;**72**:957–983. DOI: 10.1175/JAS-D-13-0370.1

[16] Y. Yasuda, K. Sato, N. Sugimoto. A theoretical study on the spontaneous radiation of inertia-gravity waves using the renormalization group method. Part II: verification of the theoretical equations by numerical simulation. J. Atmos. Sci. 2015;**72**:984–1009. DOI: 10.1175/JAS-D-13-0371.1

[17] J. Vanneste. Balance and spontanous wave generation in geophysical flows. Annu. Rev. Fluid. Mech. 2013;**45**:147–172. DOI: 10.1146/annurev-fluid-011212-140730

[18] M. E. McIntyre. Spontaneous imbalance and hybrid vortex-gravity structures. J. Atmos. Sci. 2009;**66**:1315–1325. DOI: 10.1175/2008JAS2538.1

[19] N. Sugimoto, K. Ishioka, S. Yoden. Gravity wave radiation from unsteady rotational flow in an f-plane shallow water system. Fluid. Dyn. Res. 2007;**39**(11–12):731–754. DOI: 10.1016/j.fluiddyn.2007.07.001

[20] N. Sugimoto, K. Ishioka, K. Ishii. Parameter sweep experiments on spontaneous gravity wave radiation from unsteady rotational flow in an f-plane shallow water system. J. Atmos. Sci. 2008;**65**:235–249. DOI: 10.1175/2007JAS2404.1

[21] N. Sugimoto, K. Ishii. Spontaneous gravity wave radiation in a shallow water system on a rotating sphere. J. Meteor. Soc. Japan. 2012;**90**(1):101–125. DOI: 10.2151/jmsj.2012-106

[22] N. Sugimoto, K. Ishioka, H. Kobayashi, Y. Shimomura. Cyclone-anticyclone asymmetry in gravity wave radiation from a co-rotating vortex pair in rotating shallow water. J. Fluid Mech. 2015;**772**:80–106. DOI: 10.1017/jfm.2015.209

[23] N. Sugimoto. Inertia-gravity wave radiation from the elliptical vortex in the f-plane shallow water system. Fluid. Dyn. Res. Under revision.

[24] N. Sugimoto. Inertia-gravity wave radiation from the merging of two co-rotating vortices in the f-plane shallow water system. Phys. Fluids. 2015;**27**:12701. DOI: 10.1063/1.4936869

[25] N. Sugimoto. Gravity wave radiation from asymmetric vortex merger in an f-plane shallow water system. Theor. Comput. Fluid Dyn. Forthcoming.

[26] B. E. Mitchell, S. K. Lele, P. Moin. Direct computation of the sound from a compressible co-rotating vortex pair. J. Fluid Mech. 1995;**285**:181–202. DOI: 10.1017/S0022112095000504

[27] H. Lamb. Hydrodynamics. New York: Dover; 1932. 762 p.

[28] K. Ishioka. A spectral method for unbounded domains and its application to wave equations in geophysical fluid dynamics. In: Y. Kaneda, editor. IUTAM Symposium on Computational Physics and New Perspectives in Turbulence; 11–14 September 2006; Nagoya, Japan: Springer; 2008. pp. 291–296. DOI: 10.1007/978-1-4020-6472-2_45

[29] N. Sugimoto, K. Ishioka, S. Yoden. Balance regimes for the stability of a jet in an f-plane shallow water system. Fluid. Dyn. Res. 2007;**39**(5):353–377. DOI: 10.1016/j.fluiddyn.2006.07.004